arXiv:1907.04431v1 [nucl-ex] 9 Jul 2019

Measurement of ^{139}La(p,x) Cross Sections from 35–60 MeV by Stacked-Target Activation

Jonathan T. Morrell,[1] Andrew S. Voyles,[1] M.S. Basunia,[2] Jon C. Batchelder,[2] Eric F. Matthews,[1] and Lee A. Bernstein[1]

[1] *Department of Nuclear Engineering, University of California, Berkeley, Berkeley, CA 94720, USA*

[2] *Nuclear Science Division, Lawrence Berkeley National Laboratory, Berkeley, CA 94720, USA*

(Dated: December 1, 2023)

A stacked-target of natural lanthanum foils (99.9119% ^{139}La) was irradiated using a 60 MeV proton beam at the LBNL 88-Inch Cyclotron. ^{139}La(p,x) cross sections are reported between 35–60 MeV for nine radionuclides. The primary motivation for this measurement was the need to quantify the production of ^{134}Ce. As a positron-emitting analogue of the promising medical radionuclide ^{225}Ac, ^{134}Ce is desirable for *in vivo* applications of bio-distribution assays for this emerging radiopharmaceutical. The results of this measurement were compared to the nuclear model codes TALYS, EMPIRE and ALICE (using default parameters), which showed significant deviation from the measured values.

I. INTRODUCTION

Proton-induced nuclear reactions in the several tens of MeV incident energy range are commonly used for the production of radionuclides with minimal contaminants, making them a compelling production pathway for diagnostic and therapeutic medical radionuclides [1]. Well-characterized nuclear data for many of these reactions are scarce, yet are critical for researchers wishing to optimize production schemes for these radionuclides [2].

In this work we measured cross sections for the ^{139}La(p,x) reactions, with a particular interest in the (p,6n) reaction on ^{139}La (99.9119% n.a.) for the production of ^{134}Ce, a medically relevant radionuclide. In addition, the data from this experiment provide insight into reaction mechanisms and nuclear properties, including pre-eqillibrium particle emission and nuclear level densities, making it useful for benchmarking nuclear reaction modeling codes [2–4].

I.1. Motivation

Actinium-225 is a promising candidate for new alpha-emitting therapeutic radio-pharmaceuticals [5]. Actinium-225 has a relatively short half-life of 9.9203 (3) days, and decays to ^{209}Bi (stable) through the emission of 4 α and 2 β^- particles [6–10]. The short range of these α particles is prized for sparing nearby healthy tissue while delivering a lethal dose to the site of disease [11]. There are no long-lived products in the decay chain, with the longest activity being the 3.2 h ^{209}Pb [10]. These properties make ^{225}Ac a very compelling candidate for targeted radionuclide therapy [5]. In developing biological targeting vectors for the delivery of ^{225}Ac, their selectivity must be quantified using biodistribution assays [12]. The standard for these assays is positron emission tomography (PET), which isn't possible with ^{225}Ac due to the lack of positron emission in its decay chain.

Instead, ^{134}Ce has been proposed as a positron emitting analogue of ^{225}Ac, for potential use in rapid-throughput *in vivo* biodistribution assays. Cerium-134 decays with a half-life of 3.16 (4) days, which is the closest of the β^+-emitting Cerium radionuclides to the 10 day half-life of ^{225}Ac [6, 13]. PET imaging of the ^{134}Ce uptake is performed through the daughter radionuclide ^{134}La, which β^+ decays with a short half-life (6.4 minutes) [13].

One proposed mechanism for the production of ^{134}Ce is through the ^{139}La(p,6n) reaction, using targets of natural lanthanum, which have a 99.9119% natural isotopic abundance of ^{139}La. This reaction is poorly characterized in the 35–60 MeV energy region, and the predictions of the extensively-used TALYS [14] and EMPIRE [15] nuclear reaction modeling codes differ by an order of magnitude. The discrepancies in predictions from these modern codes have profound implications for the design of targets for not only the production of ^{134}Ce, but also for the production of other radionuclides utilizing energetic proton-induced reactions. The objective of this paper is to report on a new set of cross section measurements performed using the stacked-target activation technique and use the information to not only quantify the production of ^{134}Ce, but to gauge the accuracy of several different nuclear reaction models used to predict intermediate light-ion reactions in the energy range below 60 MeV.

II. METHODOLOGY

In this work we used the stacked-target activation technique, in which one can measure a reaction cross section by quantifying the activity induced within a thin foil of known areal density, using a beam of known intensity [16, 17]. In a single irradiation, many foils can be placed in a "stack" (along with monitor foils), yielding cross section measurements at multiple energies by lowering the energy of the primary beam as it traverses the stack. In this experiment "degrader" foils were also included in the stack, to further reduce the beam energy between target foils, such that the measured cross sections fell within the 35–60 MeV range.

Following irradiation, the end-of-bombardment (EoB) activities of the various proton-induced reaction products were determined by counting the γ-rays emitted from each foil, using a well-calibrated high-purity germanium (HPGe) detector. The reaction cross section (leading to a particular product) was then calculated from the EoB activity. Many of the produced radionuclides included decay feeding from a parent also produced in the ^{139}La(p,x) reaction. Where this contribution was separable, we have reported independent cross sections, however in cases where the parent decay was unable to be measured we have reported cumulative cross sections.

The proton beam current incident upon the stack was estimated using a current integrator. However the beam current used in the calculation of cross section was determined more precisely using natural copper and aluminum monitor foils for each lanthanum foil in the stack. These foils have multiple reaction channels with well-characterized cross sections [18].

The flux-averaged proton energy at which each cross section was reported was determined using a Monte Carlo model based on the Anderson & Ziegler stopping power tables [19]. This model was optimized to give the best energy assignments using the monitor foil activation measurements, consistent with the technique proposed by Graves et al. in 2016 [16]. The areal density of each foil in the stack was determined by repeated measurements of the mass and area of each foil.

II.1. Description of Experiment

The lanthanum foils used in this experiment were of 99% purity, purchased from Goodfellow Corporation (Coraopolis, PA 15108, USA). They were cold rolled to 25 µm thickness, cut to 1" by 1" squares, and sealed in glass ampules with an inert cover gas (to prevent oxidation). Just prior to the experiment these ampules were opened, and the foils were removed and cleaned with isopropyl alcohol. The dimensions and masses of these foils were measured, and they were sealed in 3M 5413-Series Kapton polyimide film tape – each piece of tape consists of 43.2 µm of a silicone adhesive (nominal 4.79 mg/cm^2) on 25.4 µm of a polyimide backing (nominal 3.61 mg/cm^2). The copper and aluminum monitor foils were cut from 25 µm-thick sheets into 1" by 1" squares, and were also measured and sealed in Kapton tape. These foil packets were then secured over the hollow aperture of 2.25" by 2.25" aluminum sample holders (see Fig. 1), which protected the foils during handling and centered them in the beam pipe. Ten sets, each consisting of a single aluminum, copper and lanthanum foil packet, were prepared in this manner for cross section measurements at ten different energies.



FIG. 1. Photo of an individual foil packet secured to the aluminum sample holder (left) and the entire foil stack (right). The front of the stack (facing the beam) is oriented towards the right in this photo.

Multiple plates of 6061-aluminum, also 2.25" by 2.25", were placed in between each set of foil packets to degrade the beam energy by a few MeV between each foil packet, allowing cross section measurements over a range of proton energies from 35–60 MeV. Additionally, stainless steel plates (approximately 100 mg/cm^2) were placed at the front and back of the stack. Post-irradiation dose mapping of the activated stainless plates using radiochromic film (Gafchromic EBT3) confirmed that the proton beam was centered on the samples, and that the entirety of the ≈1 cm-diameter primary proton beam was contained well within the 1" by 1" borders of the foil packets, consistent with previously established techniques [16, 17].

A single ORTEC GMX Series (model GMX-50220-S) High-Purity Germanium (HPGe) detector was used in this experiment. The detector is a nitrogen-cooled coaxial n-type HPGe with a 0.5 mm beryllium window, and a 64.9 mm diameter, 57.8 mm long crystal. The energy and photopeak efficiency of the HPGe detector used in this measurement were calibrated using four standard

calibration sources of known activity (rel. error <1%): ^{137}Cs, ^{152}Eu, ^{54}Mn and ^{133}Ba. The photopeak efficiencies were also corrected for detector dead-time, as well as self-attenuation within the foils — using photon attenuation cross sections retrieved from the XCOM database [20].

II.2. Facility Overview

This experiment took place using a proton beam at the 88-Inch Cyclotron located at Lawrence Berkeley National Laboratory (LBNL) in Berkeley, California [21]. The 88-Inch Cyclotron is a variable-beam, variable-energy K=140 isochronous cyclotron, with a maximum recorded proton energy of 60 MeV and a maximum proton beam current of approximately 20 µA.

The 88-Inch Cyclotron facility has several isolated beamlines for a multitude of applications (see Fig. 2). This experiment took place in Cave 0, which has a ∼3 m beamline that is shielded from any neutron radiation produced in the cyclotron vault. The target holder for the foil stack was mounted at the end of this beamline, downstream from two bending magnets and several focusing quadrupoles in the main cyclotron vault.

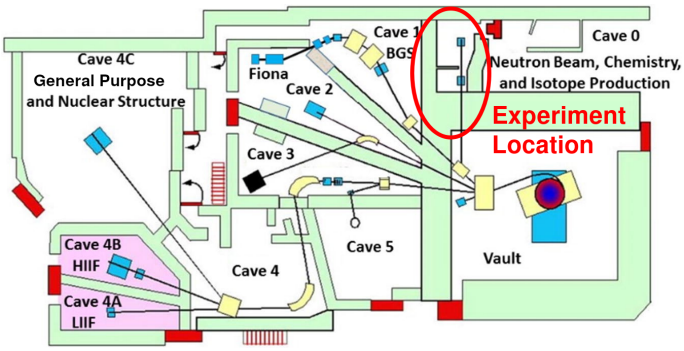


FIG. 2. Graphical representation of the 88-Inch Cyclotron floor plan. The irradiation described here took place in Cave 0, which is circled above in red.

This experiment marked the first time in recent history that the 88-Inch Cyclotron had attempted extracting a 60 MeV proton beam. Due to RF-power and beam optics limitations, the result was extremely low transmission with only approximately 8 nA of beam current (≤0.1% transmission efficiency). A subsequent tune to cave 0 exhibited significantly higher transmission, suggesting that better performance can be expected in future energetic proton runs. It was later determined by the monitor foil activation that the mean beam energy was approximately 57 MeV, and not 60 MeV as originally desired, further indicating that the initial tune was far from optimized for 60 MeV protons.

II.3. Irradiation and Counting

The foils were irradiated with 8 nA of proton beam current for 1 hour, 37 minutes and 24 seconds. The total collected charge of the beam was measured using a current integrator connected to the electrically-isolated target holder, which was used to determine that the beam current was stable over the duration of the experiment. This measurement of the beam current incident upon the target holder was also used to validate the beam current values determined using the monitor foil activation.

After irradiation, the foils were removed from the beamline and transferred to the HPGe counting lab approximately 15 minutes after EoB. Upon removal it was discovered that the third lanthanum foil showed excessive oxidation and had ruptured its Kapton encapsulation (prior to counting), indicating potential material loss. Therefore, in the interest of surety, no cross sections will be reported for this foil.

The foils were counted for four weeks following EoB. Each foil was counted multiple times, in order to reduce uncertainty and aid in isotope identification. This lengthy counting duration was necessary because the 604.6 and 606.8 keV γ-rays from the ^{135}Ce isotope significantly contaminated the 604.7 keV line emanating from the ^{134}Ce daughter isotope ^{134}La [13, 22]. Because the ^{134}Ce isotope has a longer half-life (3.16 days vs 17.7 hours), it was able to be resolved after the ^{135}Ce isotope had decayed to negligible levels [13, 22].

III. DATA ANALYSIS

The general procedure for calculating cross sections proceeded as follows. First, every γ line emitted from each isotope of interest was fit in each spectrum collected. The number of counts in each peak was used to determine the activity of the isotope at the time the spectrum was taken, and these activities as a function of "cooling" time (time since EoB) were used to calculate the EoB activity, A_0, for that isotope. Each A_0 was then used to determine a cross section (for the lanthanum foil data) or a beam current (for the copper/aluminum foil data). The energy assignments for each foil were determined using the variance minimization approach proposed by Graves [16], discussed in section III.3. The NPAT code, developed at UC Berkeley [23], was used for spectrum analysis, fitting the decay curves, and calculating the proton energy spectra in each foil.

The uncertainties in the reported cross sections had five main contributions: uncertainties in evaluated half-lives and gamma intensities (≈1%), EoB activity determination (≈1%), detector efficiency calibration (≈3%),

foil areal density (≈1%) and proton current determination (≈5%). Each contribution to the uncertainty was assumed to be independent, and was added in quadrature.

III.1. Peak Fitting

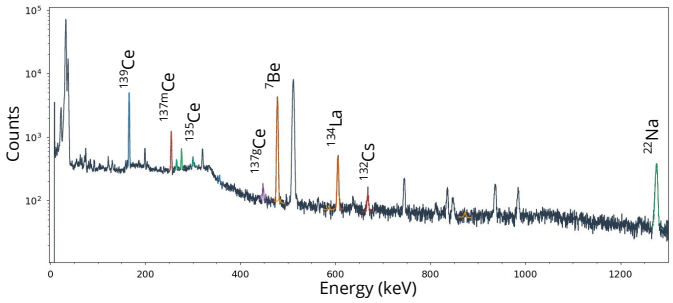


FIG. 3. A γ-ray spectrum collected from the lanthanum foil activated with approximately 56 MeV protons.

The detector energy and efficiency calibration, as well as the induced activity in each sample, were determined by peak fitting to the individual spectra. Energy centroids and relative intensities were constrained with some uncertainty by the decay data from ENSDF [24], also listed in Appendix B. Each peak was fit with a skewed Gaussian function on top of a linear background [25]. As implemented in the NPAT code [23], the complete functional form of the peak fit, $F(i)$, as a function of channel number i is as follows.

$$F_{peak}(i) = m \cdot i + b + A \cdot [\exp(-\frac{(i-\mu)^2}{2\sigma^2}) + R \cdot \exp(\frac{i-\mu}{\alpha\sigma}) \operatorname{erfc}(\frac{i-\mu}{\sqrt{2}\sigma} + \frac{1}{\sqrt{2}\alpha})] \quad (1)$$

where $m \cdot i + b$ is the background component, $A \cdot \exp(-\frac{(i-\mu)^2}{2\sigma^2})$ is the (dominant) Gaussian component, and $A \cdot R \cdot \exp(\frac{i-\mu}{\alpha\sigma}) \operatorname{erfc}(\frac{i-\mu}{\sqrt{2}\sigma} + \frac{1}{\sqrt{2}\alpha})$ is the "tailing" component. Typical values of R and α are ≈0.2 and ≈0.9, respectively.

The number of counts in a photopeak fit using this functional form is given by

$$N_c = A\left(\sqrt{2\pi}\sigma + 2R\alpha\sigma \exp(-\frac{1}{2\alpha^2})\right) \quad (2)$$

An example of a measured γ-ray spectrum is shown in Fig. 3, with photopeak fits superimposed on the spectrum.

III.2. Determining Foil Activities

To obtain the EoB activities for each proton-induced reaction product, in each foil, we determine the apparent activity from each photopeak that was observed, and perform a fit to the decay curve generated from the appropriate Bateman equations [26].

For a single photopeak having N_c counts observed with efficiency ϵ from a radionuclide with decay constant λ and intensity I_γ, the apparent activity in a photopeak at some cooling time t_c after the end-of-bombardment is given by by

$$A(t_c) = \frac{\lambda N_c}{(1 - e^{-\lambda t_m}) I_\gamma \epsilon} \quad (3)$$

where t_m is the measurement time. If the population of this nucleus has no contribution from the decay of a parent, the activity A_0 can be determined using a fit to the equation

$$A(t_c) = A_0 e^{-\lambda t_c} \quad (4)$$

Eq. 4 is only valid for single-step decay pathways, and several activation products in this experiment exhibit multi-step decays. ^{134}Ce, for example, decays to ^{134}La which then decays to the stable ^{134}Ba [13]. For these two-step decay chains, the decay curve will take the form

$$A_D(t_c) = A_{P_0} R_b \frac{\lambda_D}{\lambda_D - \lambda_P} (e^{-\lambda_P t_c} - e^{-\lambda_D t_c}) + A_{D_0} e^{-\lambda_D t_c} \quad (5)$$

where R_b is the branching-ratio, and the subscripts P and D indicate the parent and daughter isotopes respectively. An example of a fit to this exponential decay curve is shown in Fig. 4. This calculation of the EoB activities required a measurement of the initial parent activity A_{P_0}, again using a fit to Eq. 4, which somewhat increased the uncertainty in the calculation of the initial daughter activities. However, most EoB activities were still quantified to approximately 1–3% relative uncertainty.

III.3. Current Monitors and Energy Assignments

Using the end-of-bombardment activities A_0 determined by the activation spectra and the measured areal densities ρr of each foil, we can calculate the proton beam

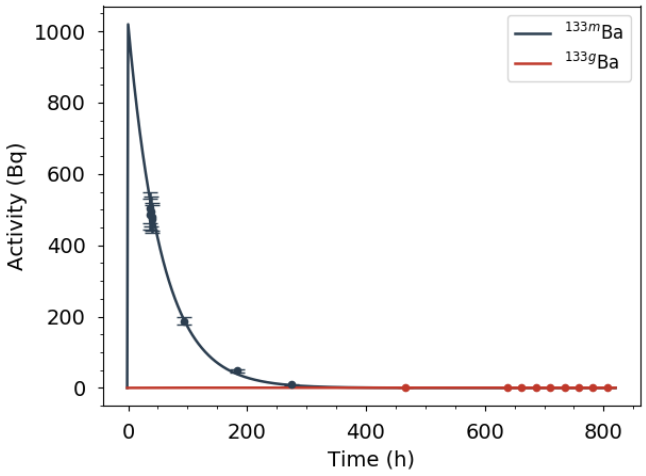


FIG. 4. Example of a decay curve and associated exponential fit used to calculate the initial activity of the ^{133m}Ba and ^{133g}Ba isotopes in the 1^{st} lanthanum foil. The uncertainty in the activity was dominated by counting statistics and the evaluated half-life for most of the observed reaction products.

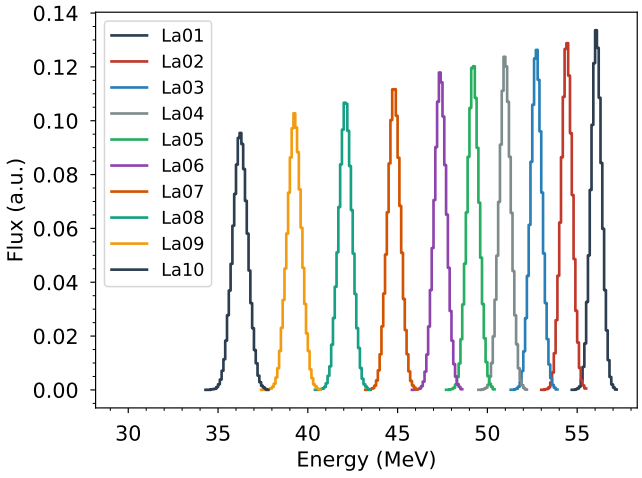


FIG. 5. Plot of the calculated proton energy spectra for each lanthanum foil in the target stack.

current (in units of protons per second), I_p, incident upon each monitor foil according to

$$I_p = \frac{A_0}{\bar{\sigma}(\rho r)(1 - e^{-\lambda t_i})} \tag{6}$$

where the factor $(1 - e^{-\lambda t_i})$ accounts for decay during a constant production interval t_i, and the flux-weighted cross section $\bar{\sigma}$ is given by

$$\bar{\sigma} = \frac{\int_0^\infty \sigma(E)\psi(E)dE}{\int_0^\infty \psi(E)dE} \tag{7}$$

where $\sigma(E)$ comes from the IAEA-recommended cross sections [27] and $\psi(E)$ is the energy spectrum of the proton flux.

This treatment accounts for the fact that the beam has a finite energy width that increases toward the back of the stack due to energy straggling of the beam. The proton flux spectrum $\psi(E)$ was determined using an Anderson & Ziegler-based Monte Carlo model, as implemented in NPAT [19, 23]. A plot showing the flux spectra for each foil in the stack, as predicted by the Anderson & Ziegler-based model, is shown in Fig. 5.

Measured currents for the three copper monitor reactions and the two aluminum reactions are plotted in Fig. 6, as well as a linear fit to these values, which was used to interpolate the beam current witnessed by the lanthanum foils. One would expect the proton beam current to decrease as it traverses the stack as the beam reacts, scatters and diffuses out of the path of downstream foils. However only a very small decrease in beam current was observed; therefore, a linear fit proved sufficient for the interpolation.

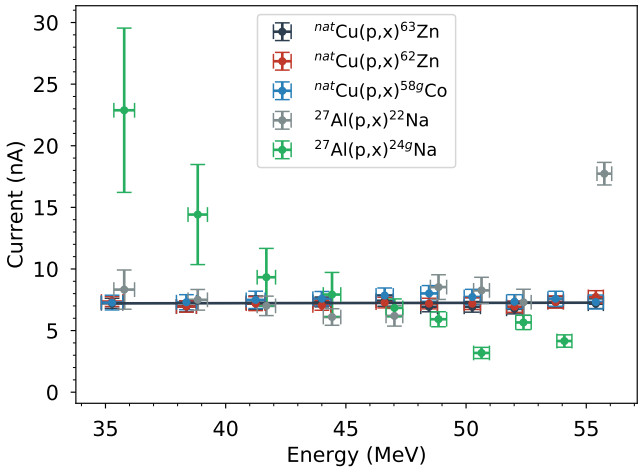


FIG. 6. Plot of the proton beam current measured by each of the monitor foil reaction channels, along with a linear fit that was used to calculate the current for the lanthanum foils.

As can be seen in Fig. 6, the uncertainty in both aluminum monitor reactions was exceptional, particularly in the ^{27}Al(p,x)^{22}Na reaction. This was due to corrections for contaminating reactions in the silicone-based adhesive of the Kapton tape that sealed the foils (^{28}Si(p,x)^{22}Na and ^{28}Si(p,x)^{24}Na), as well as reactions on the aluminum frames. These corrections were performed by measuring the activities of the ^{22}Na and ^{24}Na isotopes in the Kapton sealing the neighboring lanthanum and copper foils,

and subtracting this contribution from the aluminum foil data.

Secondary neutron production could have also contributed to ^{22,24}Na activation. However, the secondary neutron flux predicted by an MCNP model of the experiment was 3–4 orders of magnitude lower than the proton flux, suggesting that it has a minor effect on the measured monitor reaction activities [28].

To prevent systematic errors, it was decided to remove the aluminum monitor channels from the analysis, however the (post-correction) results from these channels are still plotted in Fig. 6, to illustrate the magnitude of the error induced by contaminating reactions in the aluminum frames and silicone adhesive.

III.4. Optimization of Energy Assignments

The flux-averaged proton energies and 1σ-widths of the proton energy distributions for each foil were first estimated using the Anderson & Ziegler formalism for proton transport (stack design listed in Appendix B). The apparent proton current in each monitor foil was measured using the IAEA-recommended cross sections for the ^{nat}Al(p,x)^{22}Na, ^{nat}Al(p,x)^{24}Na, ^{nat}Cu(p,x)^{62}Zn, ^{nat}Cu(p,x)^{63}Zn, and ^{nat}Cu(p,x)^{58}Co monitor reactions [27]. Disagreement in the apparent beam current between monitor channels was observed, particularly for the foils on the low energy side of the stack, which was where the energy dependence of the monitor cross sections varied most strongly. This was indicative of incorrect characterization of the proton energy spectra incident on each monitor foil.

To correct this discrepancy, the effective density of the 6061-aluminum degrader foils was treated as a free parameter in the energy loss calculation, and was optimized with respect to the reduced χ^2 of the (linear) fit to the monitor reaction data. The minimum value of χ^2_ν yields the energy assignments which give the best agreement between the proton current derived from the various monitor reaction channels. This "variance minimization" technique was performed in a manner consistent with Graves (2016) and Voyles (2018) [16, 17]. Afterwards, because the discrepancy was still quite large for foils in the high-energy portion of the stack (≈30%), the incident beam energy was also treated as a free parameter and this same minimization was performed on density and incident energy simultaneously. This resulted in a more reasonable density change of -2%, for an average incident beam energy of 57 MeV.

It should be noted that this variance minimization approach doesn't imply that the degrader density was physically less or greater than was measured, but instead serves as a correction for stopping power characterization and enhanced energy loss due to unaccounted systematics in the original stack design. In essence, this method assigns energy spectra to each foil which best match the shape of the apparent monitor reaction cross sections to the shape of the IAEA-recommended charged-particle reference standards.

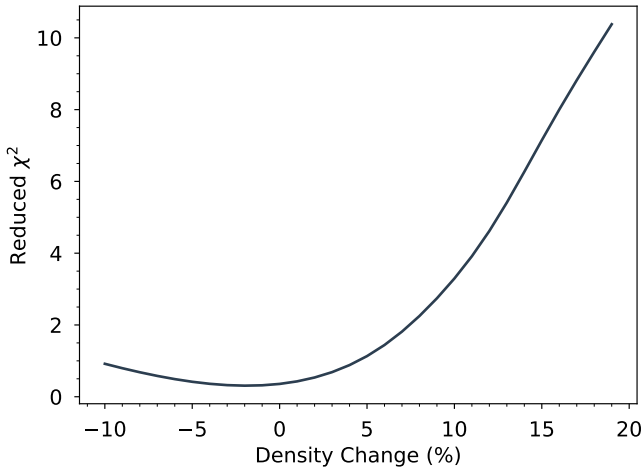


FIG. 7. Plot of the reduced χ^2 figure-of-merit for the current monitor data, as the effective density of the degraders was varied.

Fig. 7 shows the results of this minimization for an incident proton energy of 57 MeV. The reduced χ^2 of the linear fit to the monitor foil currents (shown in Fig. 6) was used to determine the optimum energy assignments, based on the Anderson & Ziegler proton transport model, by varying the effective areal density of the 6061-aluminum degraders.

This minimization shows that the optimum energy assignments result from a -2% change in the effective areal density of the stack. Additionally, it implies that the average incident proton beam energy was 57 MeV, rather than the expected 60 MeV, an unexpected deviation from the initial estimates. This discrepancy could be attributable to a number of experimental factors. This was the highest-energy proton beam in recent history at the LBNL 88-Inch Cyclotron, and the cyclotron tuning solutions were observed to be significantly different than for beams run more frequently at the facility. This is supported by the fact the transmission out of the cyclotron was very low, about 0.1%, and that a subsequent retune of the machine (after the irradiation) yielded a much better transmission.

This monitor foil variance minimization technique was also performed with the Monte Carlo code MCNP [28]. This corresponded to a 15% enhancement in the degrader areal density, which is significantly higher than comparable values in the literature [16, 17]. These results sug-

gest a systematic issue in the low-energy charged-particle stopping power tables used by MCNP, and that a detailed comparison between the Anderson & Ziegler and MCNP stopping powers should be further explored in this intermediate energy range.

IV. RESULTS AND DISCUSSION

Using the end-of-bombardment activities, beam currents, and energy assignments determined in the previous section, the flux-averaged cross sections were calculated with the following equation

$$\sigma = \frac{A_0}{I_p(\rho r)(1 - e^{-\lambda t_i})} \tag{8}$$

The results of these cross section measurements are summarized in Table I, and are described in detail below.

These results were compared to the TENDL-2017 evaluation and predictions from the TALYS-1.9, EMPIRE-3.2 and ALICE-20 nuclear reaction modeling codes, all using default parameters [14, 15, 29]. The pre-equillibrium model used in the EMPIRE and ALICE calculations was the Hybrid Monte-Carlo Simulation module (HMS), while the TALYS code uses an exciton pre-equillibrium model [14, 15, 29]. Many of the excitation functions had a characteristic "compound peak" corresponding to energies between the threshold and the opening of the next significantly populated exit channel.

These measurements were also compared to the work of Tárkányi et al., who performed a similar stacked target measurement on ^{nat}La in 2017 [30]. There were some discrepancies between the results of this work and the Tárkányi measurements, however there wasn't a clear systematic bias between one set of measurements and the other. Because the largest discrepancies were observed in channels featuring multi-step decay, it is most likely that differences in counting schedules and multi-step decay fits were the major sources of systematic discrepancies between the two experiments.

IV.1. ^{139}La(p,6n)^{134}Ce Cross Section

^{134}Ce undergoes electron capture decay to the ^{134}La ground state with a 98.9% branching ratio, with a 0.209%, 130.4 keV γ-ray being the strongest line [13]. The low-intensity and energy of this transition led us to choose the 604.721 keV (I_γ=5.04%) line in the decay of the daughter isotope ^{134}La to measure the ^{139}La(p,6n)^{134}Ce cross section. Because ^{134}La has a 6.45 minute half-life, all 604.7 keV γ's measured after several hours of decay time were attributable only to the decay of the initial ^{134}Ce population, regardless of the initial population of ^{134}La.

An additional complication was that ^{135}Ce produces multiple decay γ's very close in energy to the 604.7 keV line. Because of the 17.7 (3) hour half-life of ^{135}Ce, roughly two weeks of post-irradiation decay time were required to measure the ^{134}Ce activity without contaminating γ lines from ^{135}Ce.

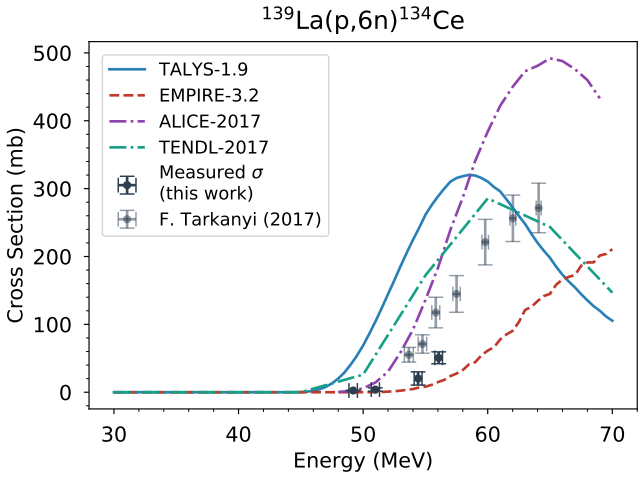


FIG. 8. Measured cross sections for the ^{139}La(p,6n)^{134}Ce reaction.

The measured cross sections for the production of ^{134}Ce are plotted in Fig. 8. The hybrid Monte Carlo simulation (HMS) pre-equillibrium model used by EMPIRE seems to slightly over-estimate the centroid energy of the "compound peak" seen in the measured data, whereas the exciton model used by TALYS underestimates the peak in the (p,6n) channel by 5–10 MeV. ALICE also uses a HMS model, and while it accurately estimates the centroid of the cross section it significantly overestimates the magnitude. This was not necessarily the case for all the measured reaction channels, but a similar trend could be seen for the (p,5n) channel as well (Fig. 9).

This was likely attributable to differences in the pre-equillibrium models between the codes. Because particles emitted in pre-equillibrium carry a significant amount of energy out of the nucleus before compound nucleus formation, small differences in these models can greatly affect which compound nucleus is formed at a given incident proton energy, shifting the centroid energy of the "compound peak". And while the TENDL-2017 evaluation (based on TALYS-1.9 [14]) better matches data than the modeling codes, it still underestimates the energy of

^{139}La(p,x) Production cross section (mb)									
E_p (MeV)	56.07(31)	54.42(32)	50.99(33)	49.21(34)	47.38(35)	44.80(37)	42.09(39)	39.25(41)	36.23(44)
^{134}Ce$_i$	50.7(88)	20.3(97)	3.9(25)	2.55(38)	-	-	-	-	-
^{135}Ce$_c$	458(23)	474(23)	377(17)	332(15)	254(14)	123.4(30)	29.00(82)	2.90(16)	0.493(37)
^{137m}Ce$_i$	79.9(47)	89.2(51)	95.9(52)	112.4(59)	124.5(75)	148.3(46)	179.9(52)	306(14)	426(14)
^{137g}Ce$_i$	23.5(51)	26.2(57)	27.4(68)	32.3(80)	37.4(74)	40.8(78)	48.7(96)	77(18)	114(30)
^{139}Ce$_c$	18.9(12)	19.1(19)	20.8(17)	17.6(16)	19.8(17)	23.9(11)	23.29(78)	31.7(16)	29.9(11)
^{132}Cs$_i$	0.170(14)	0.1114(54)	0.0405(57)	-	-	-	-	-	-
^{133m}Ba$_i$	12.54(72)	13.89(79)	13.74(74)	13.76(69)	12.57(77)	9.21(30)	5.17(15)	2.67(24)	0.682(81)
^{133g}Ba$_i$	2.82(67)	3.1(16)	2.6(13)	5.0(11)	3.4(12)	3.87(93)	1.77(58)	-	-
^{135}La$_i$	191(61)	176(77)	77(38)	77(39)	80(57)	-	-	-	-
^{nat}Cu(p,x) Production cross section (mb)									
E_p (MeV)	55.40(32) 35.28(45)	53.73(33)	52.02(34)	50.26(34)	48.46(35)	46.62(36)	44.00(38)	41.25(40)	38.37(42)
^{61}Cu$_c$	83.2(27) 182.7(44)	89.7(33)	93.0(18)	101.1(31)	110.3(37)	120.3(35)	142.4(20)	164.7(93)	183.3(72)

TABLE I. Summary of cross sections measured in this work. Subsripts c and i indicate cumulative and independant cross sections, respectively.

the peak in the cross section by about 5 MeV.

IV.2. ^{139}La(p,5n)^{135}Ce Cross Section

The ^{139}La(p,5n)^{135}Ce reaction was perhaps the most accurately quantified, due to a high number of intense γ emissions (e.g. 41.8% for the 265.56 keV line) and a 17.7 hour half-life. Because the ^{135m}Ce isomer ($t_{1/2}$=20 s) had completely decayed by the time the foils had been transferred to the counting lab, the reported cross sections for this reaction are cumulative.

The measured cross sections are plotted in Fig. 9. While TALYS and EMPIRE approximately predicted the magnitude of this cross section, the energy at which it peaks is clearly miscalculated by the TALYS exciton model. This is not surprising given the lack of low-lying level information available in ^{135}Ce in the angular momentum range that would be populated in a (p,5n) channel, with data from only a single EC-decay of ^{135}Pr and a pair of (HI,xn) measurements [31–33]. It is worth noting

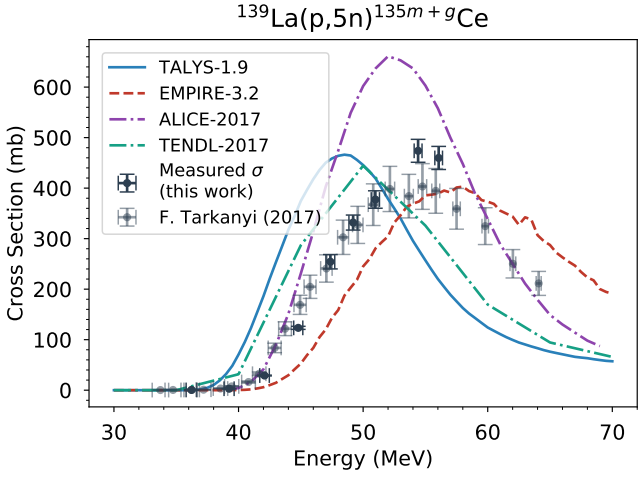


FIG. 9. Measured cross sections for the ^{139}La(p,5n)^{135}Ce reaction.

that all three models predict similar intensities for both the (p,6n) and (p,5n) channels, which together account for more than 15% of the total reaction cross section.

Due to the strong feeding of the (p,5n) channel up to 65 MeV, a higher incident energy beam (at least 70 MeV) would be required to produce ^{134}Ce for medical applications without this major contaminant.

IV.3. ^{139}La(p,3n)^{137m,g}Ce Cross Sections

The decays of both the 34.4 hour isomer and the 9.0 hour ground state in ^{137}Ce were observed, which allows for the measurement of the independent cross sections (i.e. the isomer to ground state branching ratio) for this reaction.

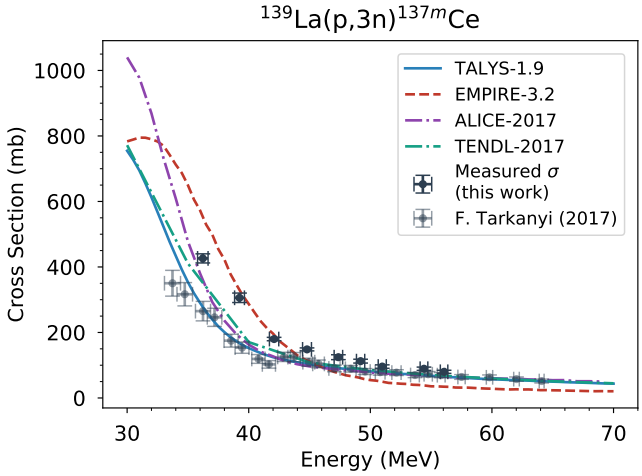


FIG. 10. Measured cross sections for the ^{139}La(p,3n)^{137m}Ce reaction.

The measured cross sections for the ^{139}La(p,3n)^{137m}Ce reaction are plotted in Fig. 10 and the ^{139}La(p,3n)^{137g}Ce cross sections are plotted in Fig. 11. In neither case is there a clear "best fit" among the models. Production of both the isomer and ground state shows better agreement with modeling codes than in the (p,5n) and (p,6n) reactions, and possibly an adjustment of the level density model or spin-cutoff parameters would bring the calculations into agreement with the data [34].

IV.4. ^{139}La(p,n)^{139}Ce Cross Section

Measurement of the direct reaction (p,n) was possible using the 80%, 165.85 keV γ emission from the ^{139}Ce ground state decay. This is reported as a cumulative cross section measurement, as the feeding from the short lived isomer ^{139m}Ce ($t_{1/2}$=58 s) could not be quantified before it had completely decayed away.

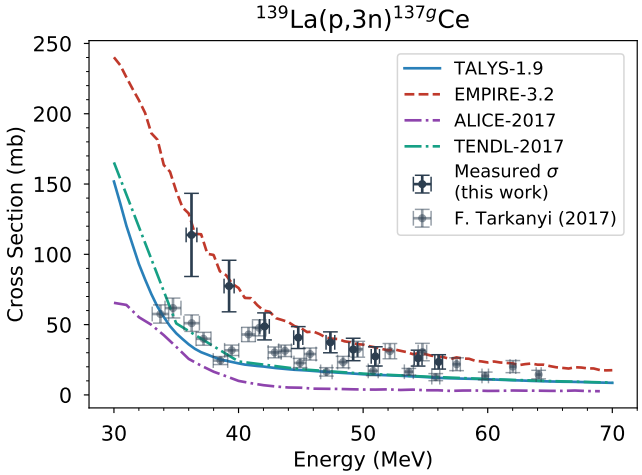


FIG. 11. Measured cross sections for the ^{139}La(p,3n)^{137g}Ce reaction.

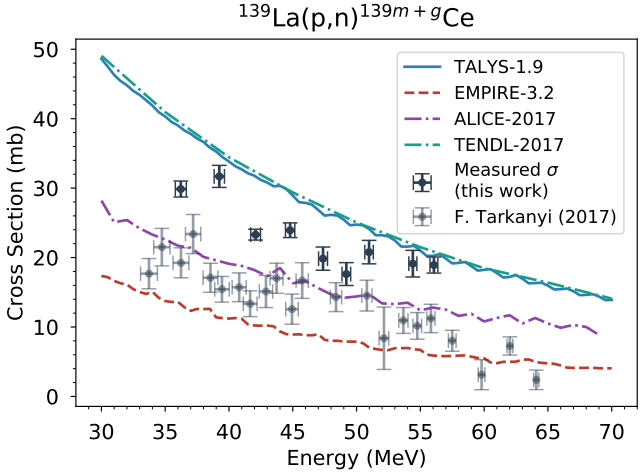


FIG. 12. Measured cross sections for the ^{139}La(p,n)^{139}Ce reaction.

The measured cross sections for the ^{139}La(p,n)^{139}Ce reaction are plotted in Fig. 12. All three models reproduce the shape of the excitation function, with ALICE being the most accurate at predicting the overall magnitude.

IV.5. ^{139}La(p,x)^{132}Cs Cross Section

Despite only producing activities on the order of 1–2 Bq, the ^{139}La(p,x)^{132}Cs reaction was measurable because its 6.48 day activity was longer lived than of most isotopes measured in this study, and because the 97.59%, 667.71 keV γ line was well isolated and could be counted

for multiple days. This provides an opportunity to study the ability of the models to predict exit channels that represent a smaller component of the overall reaction cross section.

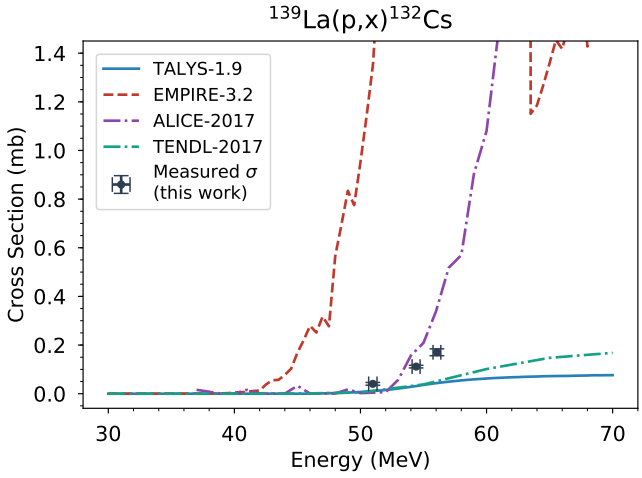


FIG. 13. Measured cross sections for the ^{139}La(p,x)^{132}Cs reaction.

Fig. 13 plots the measured ^{139}La(p,x)^{132}Cs cross sections. EMPIRE over-predicted this cross section by almost a factor of 100, whereas the TALYS calculation was far more consistent with measurements, with the ALICE prediction in between the two. The significant discrepancies seen in EMPIRE calculations are common in weakly-fed reaction channels like this one (<0.1% of total cross section), whose behavior are extremely sensitive to more dominant channels [35].

IV.6. ^{139}La(p,x)^{133m,g}Ba Cross Sections

Another reaction where the decays of both an isomer (J_π=11/2$^-$) and the ground state (J_π=1/2$^+$) were observed was the ^{139}La(p,x)^{133}Ba exit channel. The main challenge in this measurement was to identify the ^{133}Ba ground state decays, which had low activities ($\approx$ 0.1 Bq) due to the 10.55 year half-life of that isotope, and due to contaminating peaks in the spectrum for the first few weeks after the irradiation. Fortunately, the isomer has a strong peak (17.69%) at 275.92 keV, which allowed its activity to be measured with <1% uncertainty. Multiple long counts enabled the identification of the ^{133}Ba ground state and separation of the ground state activity due to the population of the isomer. Neither ^{133}Ce ($t_{1/2}$=97 (4) m) nor ^{133}La ($t_{1/2}$=3.912 (8) h) were observed in this work, both of which emit strong characteristic γ lines which would have been observable with the HPGe detector used here. Therefore, the cross sections for the ^{139}La(p,x)^{133m,g}Ba reactions are reported in this work as independent.

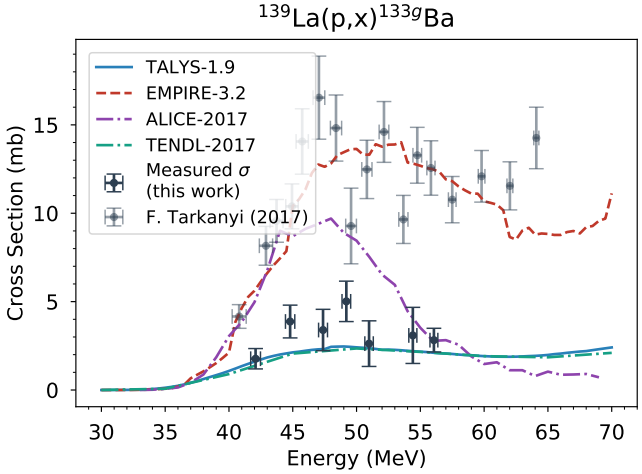


FIG. 14. Measured cross sections for the ^{139}La(p,x)^{133g}Ba reaction.

Fig. 14 plots the measured ^{139}La(p,x)^{133g}Ba reaction cross sections. The relative uncertainties were very large due to the long half-life (10.55 y) [36] and the weak feeding of this channel.

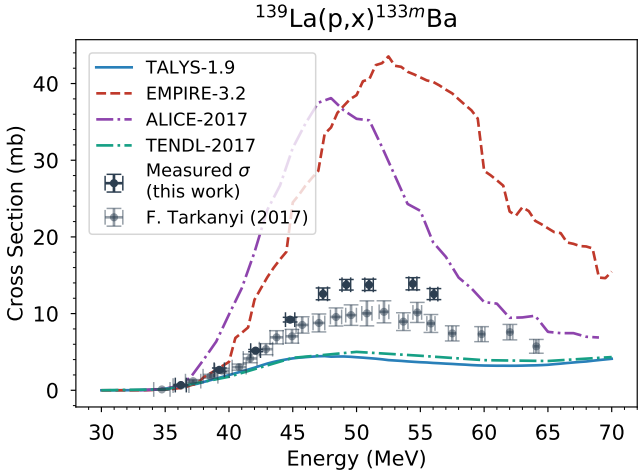


FIG. 15. Measured cross sections for the ^{139}La(p,x)^{133m}Ba reaction.

Fig. 15 plots the measured cross sections for the ^{139}La(p,x)^{133m}Ba reaction. This measurement was much more precise due to the better counting statistics from the 275.925 (7) keV line. Here again the results from EMPIRE were in better agreement with the location of the "compound peak" as a function of energy, although none of the three codes accurately predicted the magnitude of this relatively modest exit channel.

IV.7. ^{139}La(p,x)^{135}La Cross Section

The final cross section measured in the Lanthanum stack was in the ^{139}La(p,x)^{135}La reaction, which has relatively weak γ emissions but was able to be identified using the 1.52%, 480.51 keV γ line. The uncertainties in this measurement were ≈30% because the EoB ^{135}La activities were small compared to the in-feeding from ^{135}Ce decay.

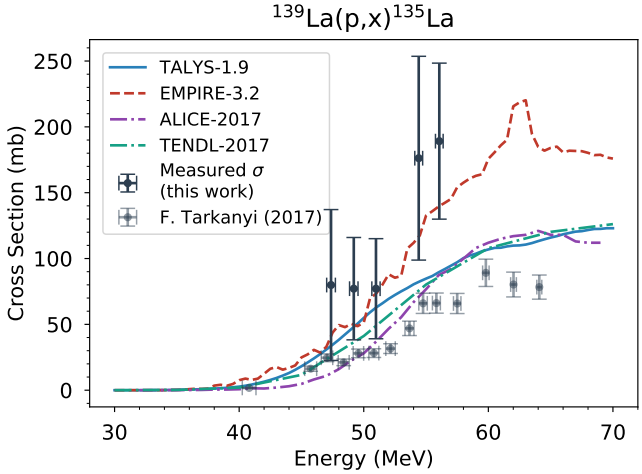


FIG. 16. Measured cross sections for the ^{139}La(p,x)^{135}La reaction.

Fig. 16 plots the measured cross sections for the ^{139}La(p,x)^{135}La reaction. The EMPIRE model once again predicts a larger magnitude than the other codes for this channel, however there is not a clear "best fit" among the three codes, particularly because of the large uncertainties in the measurements of this work.

IV.8. ^{nat}Cu(p,x)^{61}Cu Cross Section

In addition to their use in proton current determination, γ spectroscopy of the copper monitor foils provided a measurement of the ^{nat}Cu(p,x)^{61}Cu reaction through the observation of the 282.9 keV γ line (12.2%) in ^{61}Cu ($t_{1/2}$=3.339 (8) h). These measurements are plotted in Fig. 17, in comparison with literature data retrieved from the EXFOR database [16, 17, 37–42]. This measurement is consistent with literature data compiled in EXFOR, both in the shape and magnitude of the excitation function, which builds confidence in the energy and current assignments determined in this work as well as the overall measurement and data reduction methodology. Because the cross sections in this experiment are measured relative to the 2017 IAEA-recommended monitor cross sections, this measurement may be particularly useful if the

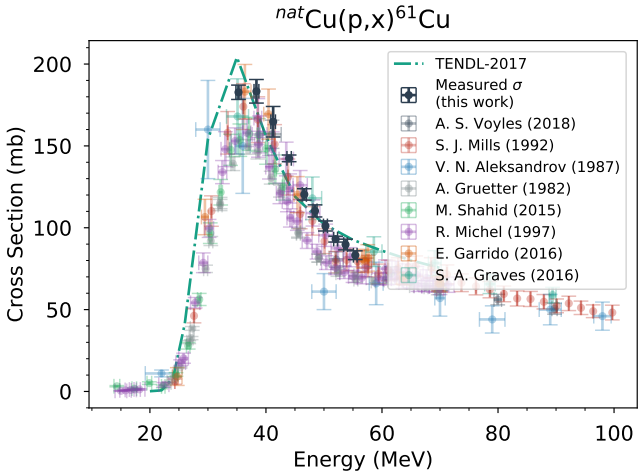


FIG. 17. Measured cross sections for the ^{nat}Cu(p,x)^{61}Cu reaction [16, 17, 37–42].

^{nat}Cu(p,x)^{61}Cu reaction were to be included in a future evaluation, which may be unlikely due to the potential for secondary neutron contamination in this channel.

V. SUMMARY AND CONCLUSIONS

In this experiment, we measured the cross sections for nine ^{139}La(p,x) reactions using a 57 MeV proton beam stacked-target irradiation at the LBNL 88-Inch Cyclotron. These measurements are compared with the outputs of the TALYS, EMPIRE and ALICE nuclear reaction modeling codes, using default parameters. In many cases, all three codes had difficulty reproducing the magnitude of the cross sections, but TALYS consistently under-predicted the energy of the "compound peak", whereas the EMPIRE and ALICE predictions tended to better reproduce the shape of the excitation functions. Better agreement with the models was found for the more strongly-fed exit channels. This illustrates the current deficiencies in reaction modeling of pre-equilibrium particle emission, which are highly sensitive to the nuclear level density and spin-distribution models employed. This systematic issue will be the subject of a forthcoming publication.

Particular emphasis was placed on the production of ^{134}Ce, a radionuclide with applications as a positron-emitting analogue of ^{225}Ac, a promising medical radionulcide. The results of this study show that in order to produce significant quantities of ^{134}Ce from the ^{139}La(p,6n) reaction, a proton beam of higher energy would be more effective. The highest-energy proton beam available at the LBNL 88-Inch Cyclotron (60 MeV) produces unacceptable quantities of other long-

lived cerium radionuclides, which must be avoided for biodistribution studies. Based on the present work, we believe that a proton beam of at least 70 MeV will be required to produce significant activities of ^{134}Ce without major contaminants.

ACKNOWLEDGEMENTS

We wish to acknowledge our thanks to the operators of the 88-Inch Cyclotron, Brien Ninemire, Nick Brickner, Tom Gimpel and Scott Small, for their efforts in setting a new "high-water mark" for the maximum proton energy extracted from the machine as well as for their assistance and support. We would also like to thank the members of the LBNL Nuclear Data group and the Nuclear Engineering department at UC Berkeley, who contributed their time and knowledge towards the review of this experiment.

This work has been performed under the auspices of the U.S. Department of Energy by Lawrence Berkeley National Laboratory under contract No. LAB16-1588 NSD. This research is supported by the U.S. Department of Energy Isotope Program, managed by the Office of Science for Nuclear Physics.

[1] F. Tárkányi, F. Ditrói, S. Takács, A. Hermanne, and M. Baba, "Activation cross sections of proton and deuteron induced nuclear reactions on holmium and erbium, related to the production of 161Er and 160Er medical isotopes," Applied Radiation and Isotopes **115**, 262 – 266 (2016).

[2] L.A. Bernstein, David Brown, Aaron Hurst, John Kelly, Filip Kondev, E Mccutchan, Caroline Nesaraja, R Slaybaugh, and Alejandro Sonzogni, "Nuclear Data Needs and Capabilities for Applications," (2015).

[3] N. Otuka, E. Dupont, V. Semkova, B. Pritychenko, A.I. Blokhin, M. Aikawa, S. Babykina, M. Bossant, G. Chen, S. Dunaeva, R.A. Forrest, T. Fukahori, N. Furutachi, S. Ganesan, Z. Ge, O.O. Gritzay, M. Herman, S. Hlavač, K. Katō, B. Lalremruata, Y.O. Lee, A. Makinaga, K. Matsumoto, M. Mikhaylyukova, G. Pikulina, V.G. Pronyaev, A. Saxena, O. Schwerer, S.P. Simakov, N. Soppera, R. Suzuki, S. Takcs, X. Tao, S. Taova, F. Tárkányi, V.V. Varlamov, J. Wang, S.C. Yang, V. Zerkin, and Y. Zhuang, "Towards a More Complete and Accurate Experimental Nuclear Reaction Data Library (EXFOR): International Collaboration Between Nuclear Reaction Data Centres (NRDC)," Nuclear Data Sheets **120**, 272 – 276 (2014).

[4] Walter Hauser and Herman Feshbach, "The Inelastic Scattering of Neutrons," Phys. Rev. **87**, 366–373 (1952).

[5] Rose A Boll, Dairin Malkemus, and Saed Mirzadeh, "Production of actinium-225 for alpha particle mediated radioimmunotherapy," Applied Radiation and Isotopes **62**, 667–679 (2005).

[6] A.K. Jain, R. Raut, and J.K. Tuli, "Nuclear Data Sheets for A = 225," Nuclear Data Sheets **110**, 1409 – 1472 (2009).

[7] Ashok Kumar Jain, Sukhjeet Singh, Suresh Kumar, and Jagdish K. Tuli, "Nuclear Data Sheets for A = 221," Nuclear Data Sheets **108**, 883 – 922 (2007).

[8] F.G. Kondev, E.A. McCutchan, B. Singh, K. Banerjee, S. Bhattacharya, A. Chakraborty, S. Garg, N. Jovancevic, S. Kumar, S.K. Rathi, T. Roy, J. Lee, and R. Shearman, "Nuclear Data Sheets for A=217," Nuclear Data Sheets **147**, 382 – 458 (2018).

[9] M.S. Basunia, "Nuclear Data Sheets for A = 213," Nuclear Data Sheets **108**, 633 – 680 (2007).

[10] J. Chen and F.G. Kondev, "Nuclear Data Sheets for A = 209," Nuclear Data Sheets **126**, 373 – 546 (2015).

[11] Deborah A Mulford, David A Scheinberg, and Joseph G Jurcic, "The Promise of Targeted alpha-Particle Therapy," Journal of Nuclear Medicine **46**, 199S———204S (2005).

[12] C. Apostolidis, R. Molinet, G. Rasmussen, and A. Morgenstern, "Production of Ac-225 from Th-229 for Targeted alpha Therapy," Analytical Chemistry **77**, 6288–6291 (2005), pMID: 16194090, https://doi.org/10.1021/ac0580114.

[13] A.A. Sonzogni, "Nuclear Data Sheets for A = 134," Nuclear Data Sheets **103**, 1 – 182 (2004).

[14] A J Koning and D Rochman, "Modern Nuclear Data Evaluation with the TALYS Code System," Nuclear Data Sheets **113**, 2841–2934 (2012).

[15] M. Herman, R. Capote, B.V. Carlson, P. Obložinský, M. Sin, A. Trkov, H. Wienke, and V. Zerkin, "EMPIRE: Nuclear Reaction Model Code System for Data Evaluation," Nuclear Data Sheets **108**, 2655 – 2715 (2007), special Issue on Evaluations of Neutron Cross Sections.

[16] Stephen A. Graves, Paul A. Ellison, Todd E. Barnhart, Hector F. Valdovinos, Eva R. Birnbaum, Francois M. Nortier, Robert J. Nickles, and Jonathan W. Engle, "Nuclear excitation functions of proton-induced reactions (Ep=35–90MeV) from Fe, Cu, and Al," Nuclear Instruments and Methods in Physics Research Section B: Beam Interactions with Materials and Atoms **386**, 44 – 53 (2016).

[17] Andrew S. Voyles, Lee A. Bernstein, Eva R. Birnbaum, Jonathan W. Engle, Stephen A. Graves, Toshihiko Kawano, Amanda M. Lewis, and Francois M. Nortier, "Excitation functions for (p,x) reactions of niobium in the energy range of Ep=40–90MeV," Nuclear Instruments and Methods in Physics Research Section B: Beam Interactions with Materials and Atoms **429**, 53 – 74 (2018).

[18] IAEA, "Charged Particle Cross-Section Database for Medical Radioisotope Production: Diagnostic Radioisotopes and Monitor Reactions Final Report of a Coordinated Research Project," International Atomic Energy Agency, Vienna, Austria (2001).

[19] James F. Ziegler, M.D. Ziegler, and J.P. Biersack, "SRIM The stopping and range of ions in matter (2010)," Nuclear Instruments and Methods in Physics

Research Section B: Beam Interactions with Materials and Atoms **268**, 1818 – 1823 (2010), 19th International Conference on Ion Beam Analysis.

[20] M J Berger, J H Hubbell, S M Seltzer, J Chang, J S Coursey, R Sukumar, D S Zucker, and K Olsen, "XCOM: Photon cross section database (version 1.5)," (2010).

[21] M. Kireeff Covo, R.A. Albright, B.F. Ninemire, M.B. Johnson, A. Hodgkinson, T. Loew, J.Y. Benitez, D.S. Todd, D.Z. Xie, T. Perry, L. Phair, L.A. Bernstein, J. Bevins, J.A. Brown, B.L. Goldblum, M. Harasty, K.P. Harrig, T.A. Laplace, E.F. Matthews, A. Bushmaker, D. Walker, V. Oklejas, A.R. Hopkins, D.L. Bleuel, J. Chen, and S.B. Cronin, "The 88-Inch Cyclotron: A one-stop facility for electronics radiation and detector testing," Measurement **127**, 580 – 587 (2018).

[22] Balraj Singh, Alexander A. Rodionov, and Yuri L. Khazov, "Nuclear Data Sheets for A = 135," Nuclear Data Sheets **109**, 517 – 698 (2008).

[23] Jonathan T. Morrell, "NPAT: Nuclear physics analysis tools," (2019–), [Online; accessed June 25, 2019.].

[24] M. R. Bhat, "Evaluated nuclear structure data file (ensdf)," in *Nuclear Data for Science and Technology*, edited by Syed M. Qaim (Springer Berlin Heidelberg, Berlin, Heidelberg, 1992) pp. 817–821.

[25] Glenn Knoll, *Radiation Detection and Measurement* (John Wiley & Sons, Inc., 1999) pp. 425–435.

[26] H. Bateman, "The solution of a system of differential equations occurring in the theory of radioactive transformations," In Proc. Campridge Philos. Soc. **15**, 423 – 427 (1910).

[27] A Hermanne, A V Ignatyuk, R Capote, B V Carlson, J W Engle, M A Kellett, T Kibédi, G Kim, F G Kondev, M Hussain, O Lebeda, A Luca, Y Nagai, H Naik, A L Nichols, F M Nortier, S V Suryanarayana, S Takács, F T Tárkányi, and M Verpelli, "Reference Cross Sections for Charged-particle Monitor Reactions," Nuclear Data Sheets **148**, 338–382 (2018).

[28] T E Booth F B Brown J S Bull L J Cox J W J Durkee J S Elson M L Fensin R A I Forster J S Hendricks H G I Hughes R C Johns B C Kiedrowski R L Martz S G Mashnik G W McKinney D B Pelowitz R E Prael J E Sweezy L S Waters T Wilcox A J Zukaitis J.T. Goorley M.R. James, John T Goorley, Michael R James, Thomas E Booth, Forrest B Brown, Jeffrey S Bull, Lawrence J Cox, Joe W Jr. Durkee, Jay S Elson, Michael Lorne Fensin, Robert A I I I Forster, John S.; Hendricks, H Grady I I I Hughes, Russell C Johns, Brian C Kiedrowski, Roger L Martz, Stepan G Mashnik, Gregg W McKinney, Denise B.; Pelowitz, Richard E Prael, Jeremy Ed Sweezy, Laurie S Waters, Trevor Wilcox, Anthony J Zukaitis, T Goorley, Michael R James, Thomas E Booth, Forrest B Brown, Jeffrey S Bull, Lawrence J Cox, Joe W Jr. Durkee, Jay S Elson, Michael Lorne Fensin, Robert A I I I Forster, John S.; Hendricks, H Grady I I I Hughes, Russell C Johns, Brian C Kiedrowski, Roger L Martz, Stepan G Mashnik, Gregg W McKinney, Denise B.; Pelowitz, Richard E Prael, Jeremy Ed Sweezy, Laurie S Waters, Trevor Wilcox, and T Zukaitis, "Initial MCNP6 release Overview - MCNP6 version 1.0," Los Alamos Report LA-UR-13-22934 **180**, 298–315 (2013).

[29] M. Blann and J. Bisplinghoff, "Code ALICE/LIVERMORE 82," (1982).

[30] F Tárkányi, A Hermanne, F Ditrói, and S Takács, "Activation cross section data of proton induced nuclear reactions on lanthanum in the 3465 MeV energy range and application for production of medical radionuclides," Journal of Radioanalytical and Nuclear Chemistry **312**, 691–704 (2017).

[31] R Alt, G Beyer, VA Morozov, H Musiol, TM Numinov, H Tyrroff, H Strusny, ZA Usmanova, VI Fominykh, H Fuya, *et al.*, "On the 135pr-135ce decay scheme," Izv. Akad. Nauk SSSR, Ser. Fiz. **36**, 744 (1972).

[32] R. Ma, E. S. Paul, D. B. Fossan, Y. Liang, N. Xu, R. Wadsworth, I. Jenkins, and P. J. Nolan, "Rotational bands in ^{135}ce: Collective prolate and oblate rotation," Phys.Rev. **C41**, 2624 (1990).

[33] H. C. Jain, S. Lakshmi, and P. K. Joshi, "Identification of chiral bands in ^{135}ce," in *Proc.Nuclei at the Limits* (2005).

[34] D.M. Brink, "Individual particle and collective aspects of the nuclear photoeffect," Nuclear Physics **4**, 215 – 220 (1957).

[35] A J Koning and J P Delaroche, "Local and global nucleon optical models from 1 keV to 200 MeV," Nuclear Physics A **713**, 231–310 (2003).

[36] Yu. Khazov, A. Rodionov, and F.G. Kondev, "Nuclear Data Sheets for A = 133," Nuclear Data Sheets **112**, 855 – 1113 (2011).

[37] A. Grütter, "Excitation functions for radioactive isotopes produced by proton bombardment of Cu and Al in the energy range of 16 to 70 MeV," Nuclear Physics A **383**, 98 – 108 (1982).

[38] VN Aleksandrov, MP Semyonova, and VG Semyonov, "Excitation functions for radionuclides produced by (p, x) reactions of copper and nickel," Atomnaya Energiya **62**, 411 (1987).

[39] S.J. Mills, G.F. Steyn, and F.M. Nortier, "Experimental and theoretical excitation functions of radionuclides produced in proton bombardment of copper up to 200 MeV," International Journal of Radiation Applications and Instrumentation. Part A. Applied Radiation and Isotopes **43**, 1019 – 1030 (1992).

[40] R. Michel, R. Bodemann, H. Busemann, R. Daunke, M. Gloris, H.-J. Lange, B. Klug, A. Krins, I. Leya, M. Lpke, S. Neumann, H. Reinhardt, M. Schnatz-Bttgen, U. Herpers, Th. Schiekel, F. Sudbrock, B. Holmqvist, H. Cond, P. Malmborg, M. Suter, B. Dittrich-Hannen, P.-W. Kubik, H.-A. Synal, and D. Filges, "Cross sections for the production of residual nuclides by low- and medium-energy protons from the target elements C, N, O, Mg, Al, Si, Ca, Ti, V, Mn, Fe, Co, Ni, Cu, Sr, Y, Zr, Nb, Ba and Au," Nuclear Instruments and Methods in Physics Research Section B: Beam Interactions with Materials and Atoms **129**, 153 – 193 (1997).

[41] Muhammad Shahid, Kwangsoo Kim, Haladhara Naik, Muhammad Zaman, Sung-Chul Yang, and Guinyun Kim, "Measurement of excitation functions in proton induced reactions on natural copper from their threshold to 43MeV," Nuclear Instruments and Methods in Physics Research Section B: Beam Interactions with Materials and Atoms **342**, 305 – 313 (2015).

[42] E. Garrido, C. Duchemin, A. Guertin, F. Haddad, N. Michel, and V. Métivier, "New excitation functions for proton induced reactions on natural titanium, nickel and copper up to 70MeV," Nuclear Instruments and Methods in Physics Research Section B: Beam Interactions with Materials and Atoms **383**, 191 – 212 (2016).

[43] E. Browne and J.K. Tuli, "Nuclear Data Sheets for A =

137," Nuclear Data Sheets **108**, 2173 – 2318 (2007).
[44] Paresh K. Joshi, Balraj Singh, Sukhjeet Singh, and Ashok K. Jain, "Nuclear Data Sheets for A = 139," Nuclear Data Sheets **138**, 1 – 292 (2016).
[45] Yu. Khazov, A.A. Rodionov, S. Sakharov, and Balraj Singh, "Nuclear Data Sheets for A=132," Nuclear Data Sheets **104**, 497 – 790 (2005).
[46] Kazimierz Zuber and Balraj Singh, "Nuclear Data Sheets for A = 61," Nuclear Data Sheets **125**, 1 – 200 (2015).
[47] Alan L. Nichols, Balraj Singh, and Jagdish K. Tuli, "Nuclear Data Sheets for A = 62," Nuclear Data Sheets **113**, 973 – 1114 (2012).
[48] Bai Erjun and Huo Junde, "Nuclear Data Sheets for A = 63," Nuclear Data Sheets **92**, 147 – 252 (2001).
[49] Caroline D. Nesaraja, Scott D. Geraedts, and Balraj Singh, "Nuclear Data Sheets for A = 58," Nuclear Data Sheets **111**, 897 – 1092 (2010).
[50] M. Shamsuzzoha Basunia, "Nuclear Data Sheets for A = 22," Nuclear Data Sheets **127**, 69 – 190 (2015).
[51] R.B. Firestone, "Nuclear Data Sheets for A = 24," Nuclear Data Sheets **108**, 2319 – 2392 (2007).

Appendix A: Stack Design

Foil Id	Compound	Δx (mm)	$\rho\Delta x$ (mg/cm^2)
SS3	316 SS	0.13	100.48 ± 0.46
La01	La	0.0275	14.59 ± 0.69
Al01	Al	0.027	6.58 ± 0.02
Cu01	Cu	0.029	22.13 ± 0.07
E1	Al	0.254	68.53 ± 5.08
La02	La	0.0278	15.55 ± 0.71
Al02	Al	0.0278	6.67 ± 0.12
Cu02	Cu	0.0293	22.23 ± 0.44
E2	Al	0.254	68.53 ± 5.08
La03	La	0.0315	15.12 ± 0.83
Al03	Al	0.027	6.7 ± 0.03
Cu03	Cu	0.031	22.24 ± 0.07
E3	Al	0.254	68.53 ± 5.08
La04	La	0.0288	14.95 ± 0.66
Al04	Al	0.027	6.68 ± 0.03
Cu04	Cu	0.0317	22.49 ± 0.42
E4	Al	0.254	68.53 ± 5.08
La05	La	0.027	15.07 ± 0.65
Al05	Al	0.027	6.64 ± 0.01
Cu05	Cu	0.0313	22.39 ± 0.42
E5	Al	0.254	68.53 ± 5.08
La06	La	0.026	14.32 ± 0.78
Al06	Al	0.0278	6.66 ± 0.23
Cu06	Cu	0.031	22.22 ± 0.05
E6+E7	Al	0.508	137.06 ± 10.16
La07	La	0.0258	14.21 ± 0.29
Al07	Al	0.0273	6.64 ± 0.12
Cu07	Cu	0.031	22.4 ± 0.05
E8+E9	Al	0.508	137.06 ± 10.16
La08	La	0.0283	15.64 ± 0.28
Al08	Al	0.0273	6.72 ± 0.13
Cu08	Cu	0.032	22.16 ± 1.2
E10+E11	Al	0.508	137.06 ± 10.16
La09	La	0.0268	12.67 ± 0.51
Al09	Al	0.0275	6.65 ± 0.14
Cu09	Cu	0.031	22.2 ± 0.72
E12+E13	Al	0.508	137.06 ± 10.16
La10	La	0.0278	16.14 ± 0.3
Al10	Al	0.027	6.73 ± 0.02
Cu10	Cu	0.031	22.5 ± 0.05
SS4	316 SS	0.13	101.26 ± 0.79

Appendix B: Relevant Nuclear Data [13, 22, 36, 43–51]

Isotope	γ Energy (keV)	I_γ (%)	$T_{1/2}$
^{134}Ce	-	-	3.16 (4) d
^{134}La	604.721 (2)	5.04 (20)	6.45 (16) m
^{135}Ce	265.56 (2)	41.8 (14)	17.7 (3) h
^{137m}Ce	254.29 (5)	11.1 (4)	34.4 (3) h
^{137g}Ce	447.15 (8)	1.68 (6)	9.0 (3) h
^{139g}Ce	165.8575 (11)	79.95 (6)	137.64 (2) d
^{135}La	480.51 (2)	1.52 (24)	19.5 (2) h
^{133m}Ba	275.925 (7)	17.69 (25)	38.93 (1) h
^{133g}Ba	356.0129 (7)	62.05 (19)	10.551 (11) y
^{132}Cs	667.714 (2)	97.59 (9)	6.480 (6) d
^{61}Cu	282.956 (10)	12.2 (22)	3.339 (8) h
^{62}Zn	596.56 (13)	26.0 (20)	9.193 (15) h
^{63}Zn	669.62 (5)	8.2 (3)	38.47 (5) m
^{58}Co	810.7593 (20)	99.45 (1)	70.86 (6) d
^{22}Na	1274.537 (7)	99.940 (14)	2.6018 (22) y
^{24}Na	1368.626 (5)	99.9936 (15)	14.997 (12) h